A Model of Using the Asymmetric Polydopamine Thin Film for Mimicking Epithelial Folding In Vitro

Yan Nie,, Yue Liu, Xun Xu, Weiwei Wang, Nico Scharnagl, Matthias Heuchel, Andreas Lendlein,* and Nan Ma*

The basement membrane (BM) is a biointeractive ultrathin network with distinct composition and organization of its epithelial and stromal sides, which render BMs with asymmetric biofunctions and mechanical properties. There are difficulties in the recapitulation of the highly hierarchical structure and function of BM. Here, the interfacial assembly method for the generation of BM mimics is applied. Dopamine is the starting material for the polymerization and assembly of polydopamine (PDA) into asymmetric materials. Compared to the PDA coating formed at the solid/liquid interface (≈20 nm), the PDA film formed at the air/liquid interface displays a thickness of ≈100 nm. Moreover, it possesses an asymmetric surface topography and an apparent Young's modulus of ≈1.0 MPa, which is structurally and mechanically similar to natural BMs. Of interest, the airside and the waterside of the PDA film exhibit differences in their adhesion affinity to the human skin keratinocytes. With stronger active mechanical processes between living cells and the waterside of PDA film, epithelial folding could be mimicked. Together, the PDA film is able to recapitulate the structural and mechanical complexity of natural BMs, indicating the prospective future of using PDA films for in vitro modeling cell-BM interaction and tissue formation.

Y. Nie, Y. Liu, X. Xu, W. Wang, M. Heuchel, A. Lendlein, N. Ma
Institute of Active Polymers
Helmholtz-Zentrum
14513 Hereon, Germany
E-mail: lendlein@uni-potsdam.de; nan.ma@hereon.de
N. Scharnagl
Institute of Surface Science
Helmholtz-Zentrum
21502 Hereon, Germany
A. Lendlein
Institute of Chemistry
University of Potsdam
14476 Potsdam, Germany
N. Ma
Institute of Chemistry and Biochemistry
Free University of Berlin
14195 Berlin, Germany

The ORCID identification number(s) for the author(s) of this article can be found under https://doi.org/10.1002/admi.202202509.

1. Introduction

The skin basement membrane (BM) is a thin specialized network of extracellular matrix (ECM) macromolecules that connect the basal epidermal cells to the underlying dermis of stromal cells.[1] It possesses a highly organized micro-architecture characterized by its ultrathin thickness (≈100 nm), the structural and compositional asymmetry between its epithelial and stromal sides, and the micrometer-scale undulating patterns.[1b,2] The skin BM functions as the anchorage site to promote cell adhesion, a signaling hub to regulate cell functions, as well as the physical barrier to facilitate the hierarchy of compartmentalization during development.[1b,3] As a result, there is growing interest in developing BM mimics for use in tissue engineering and regenerative medicine applications.[4]

Although mounting evidence demonstrated that altering the biochemical composition of the artificial BM could change its activity and function, the crucial role of modulating the physical properties of BM mimics in the regulation of cell behaviors has only been acknowledged recently.[1b,4b] For instance, polydimethylsiloxane (PDMS) has been utilized as a scaffold to replicate the elastic properties of the BM, since the elastic properties of the PDMS can be fine-tuned by controlling the crosslinking level during fabrication.[2] Furthermore, to mimic the barrier function of BM, the PDMS has been processed into freestanding membranes with a thickness of ≈10.0 μm to investigate the rheological behavior of human epithelial cells.[5] To bring it closer to native BM dimensions (≈100 nm), a nanofiber mesh with a thickness of 2.0 μm was fabricated by electrospinning using poly(ε-caprolactone) and polyethylene glycols.[4a] Although the barrier and separation function of BM can be mimicked, those BM mimics are biochemically inert and biophysically rigid, which failed to realize cell-mediated compositionally and structurally remodeling of BM.[6] One possible solution at the structural level would be a further decrease of the membrane thickness to the nanoscale. This will render the resulting membrane more flexible, which enables the actively mechanical remodeling of BM mimics by cells. Since the bendability (b) of material depends on its overall chemical properties that determine the maximum fracture strain (ε_f) and its thickness (h)[7]

$$b = \frac{2\varepsilon_f}{h} \tag{1}$$

Beyond the BM elasticity and thickness, novel BM mimics with a more detailed structure of BM topography is still emerging. The Janus membrane with asymmetric wettability has been developed to mimic the asymmetric characteristics of BM in guiding different cell functions at the dermal-epidermal interface.[8] However, it is difficult to replicate the multifunctionality of the BM using a single polymer system currently. Moreover, as a biointeractive material, BM is not a static network, which is continually being produced and remodeled by cells through protein synthesis/degradation or reorganization, which makes the in vitro mimic of BM more challenging.

In this study, we explore the possibility of using a single polymer system to mimic multiple functions of the BM. The dopamine (DA) was selected as the starting material to synthesize the polydopamine (PDA) as the BM mimic, since PDA has been demonstrated as a highly adhesive surface and thus promotes cell proliferation.[9] The resulting PDA materials were formed either at the liquid/solid (L/S) or the air/liquid (A/L) interface, given the fact that the interfacial assembly has been identified as one of the most prevailing platforms to guide the formation of such ultrathin, flexible, and asymmetric membranes.[10] Compared to those under mechanical stimuli,[11] the PDA films generated under a static condition featured a mon-olayer "Janus" properties, where the airside and waterside of the film presented distinct surface topography and chemistry. Notably, the lower mechanical strength of the monolayer film provides the feasibility to use it to mimic the natural epithelial tissue. The PDA film-cell system could serve as a precise in vitro model system to recapitulate the wrinkling and folding of skin during wound healing and development, and to investigate the complex cell-BM interaction.

2. Result and Discussion

2.1. Substrate Functionalization with PDA

The PDA materials were synthesized through the polymerization of DA in Tris-HCl buffer (pH = 8.5, Figure S1, Supporting Information). The oxygen (O_2) concentration gradient due to molecule diffusion was designed to control the oxidation of DA.[12] Here, the resulting PDA materials were obtained at either the L/S interface (PDA coating) or the A/L interface (PDA film) after 24 h of reaction (shown in **Figure 1**A). The observation at the A/L interface and the scanning electron microscopy (SEM) cross-sectional image demonstrated that the PDA film is a freestanding flexible film (Figure 1A). The topography and the thickness of the resulting PDA materials were determined by atomic force microscope (AFM) after transferring to the thermal oxide silicon (Si/SiO_2) wafer (Figure 1B,C).
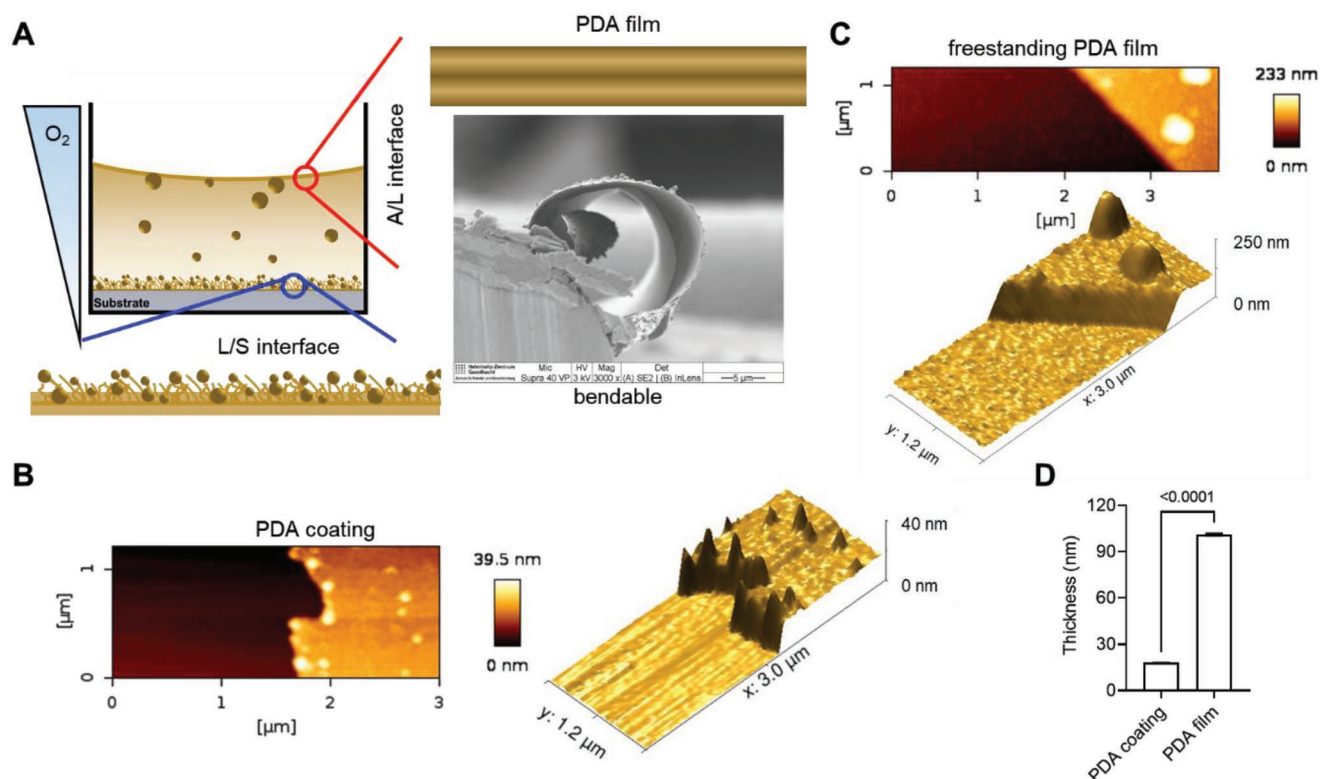

Figure 1. PDA materials formed at the A/L or L/S interface. A) Schematic illustration of the self-polymerization of DA into PDA. The resulting material could form a PDA coating layer at the L/S interface and a freestanding bendable PDA film at the A/L interface imaged by SEM. Topography of B) the PDA coating formed at the L/S interface and C) the PDA film formed at the A/L interface measured by AFM. D) Thickness of the PDA materials measured by AFM. Three height profiles of each AFM image were used to calculate the average thickness of the PDA layer.

**ADVANCED
SCIENCE NEWS**

www.advancedsciencenews.com

**ADVANCED
MATERIALS
INTERFACES**

www.advmatinterfaces.de

Larger PDA aggregates were found attached to the PDA films than to the PDA coating, indicating a higher oxidation/polymerization rate at the A/L interface than at the L/S interface. Moreover, using the scratching method, the thickness of the PDA film (101.07 ± 0.83 nm) formed at the A/L interface was found approximately five times thick as the PDA coating (17.96 ± 0.10 nm) formed at the L/S interface (Figure 1D). Comparing the A/L and L/S interfaces, the interfacial properties of those surfaces, such as surface energy, hydrophilicity/hydrophobicity, and roughness, can affect the adsorption and orientation of the dopamine molecules, as well as the subsequent polymerization and crosslinking reactions that occur during the PDA layer formation.[13] Except for the properties of the different interfaces, ambient factors, such as temperature, O_2 concentration, pH, and mechanical stimulus, also affect the structure of the resulting PDA materials.[9,12,14] For instance, the higher O_2 concentration at the A/L interface than at the L/S interface facilitated the DA oxidation and speeded up the self-assembly of the PDA, which led to the difference in their morphology and thickness.[15]

2.2. Chemical and Physical Properties of the PDA-Modified Surfaces

The suspended PDA film over the large open area also indicated the close packing and the strong lateral cohesion of the PDA layer, which allowed manipulating the orientation of the PDA film using Langmuir technology. The successful continuous PDA film transfer enabled the study of the asymmetry of the two opposing sides of the PDA film. Specifically, we described the bottom surface of the PDA film that was orientated toward the DA subphase as the waterside, while the top surface of the PDA film that was directed toward air was defined as the airside. Considering its high sensitivity in the discrimination of covalent bonds changes and the characterization of structural complexity, the Confocal Raman Spectroscopy was employed to detect the difference between the nonpolymerized DA monomer and the polymerized PDA coating, the waterside as well as the airside of PDA film (**Figure 2**A,B). The DA spectra displayed multiple peaks with the 600–1300 cm^{-1} region, indicating aliphatic chains,
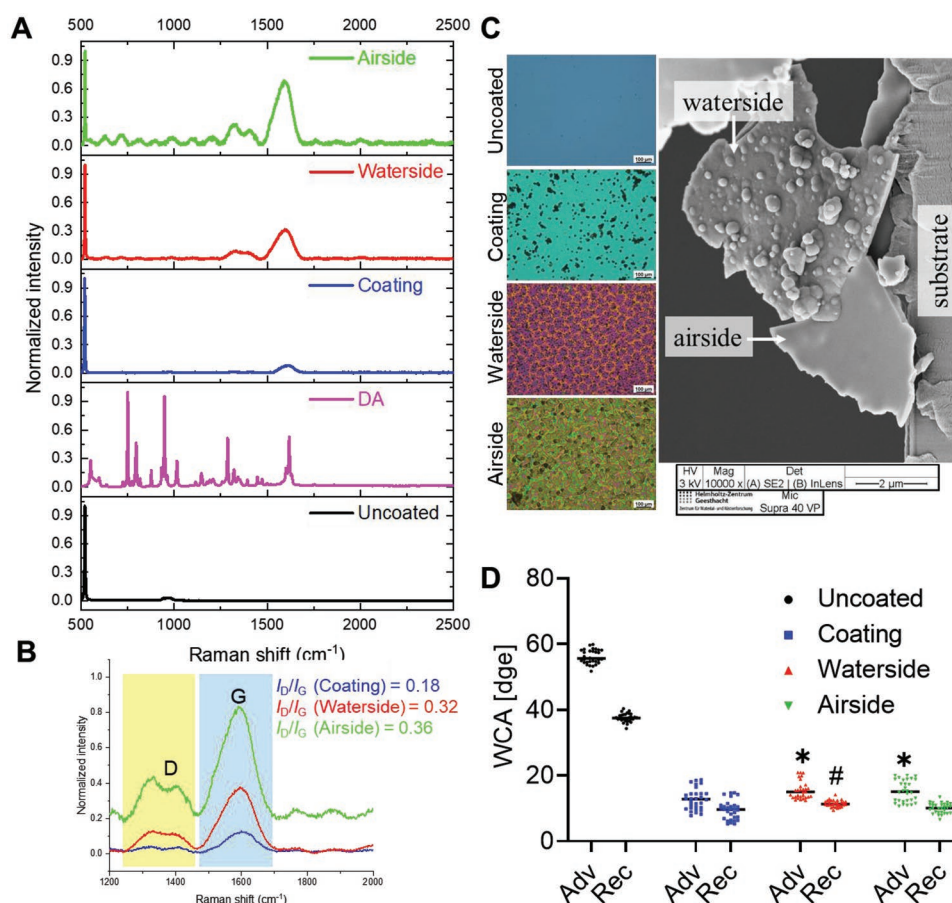
Figure 2. Physical and chemical properties of PDA-functionalized surfaces. A) Raman spectra of DA and PDA materials on Si/SiO₂ wafer. B) The peak intensity ratio of the D-band to that of the G-band (I_D/I_G ratio) of the PDA materials. C) Surface morphology of the PDA-functionalized Si/SiO₂ wafer. Optical image (left) was acquired with a digital microscope with a 3000 × magnification with a scale bar = 100 µm and the zoom-in image (right) was acquired with the SEM. D) Advancing (Adv) and receding (Rec) water contact angle (WCA) of the different PDA surfaces. For each group, three independent samples were used, on which ten randomly selected areas were measured ($n = 30$, Adv *$p < 0.01$, Rec #$p < 0.0001$, compared to the coating group).

2202509 (3 of 11)

which showed high similarity to previous measurements.[16] The Raman spectra of PDA coating and PDA films showed typical Raman shifts due to catechol stretching vibrations that evidenced the polymerization of DA into PDA, which was in line with previous studies (two main bands at ≈1360 and ≈1588 cm^{-1}).[17] Yet there was a slight difference in the shift of G peaks between PDA coating, airside, and waterside of PDA films (Figure 2A).

In addition, the major application of PDA functionalization was achieved by PDA coating that formed at the L/S interface, yet the properties of PDA films acquired at the A/L interface are not fully understood yet. It is of interest to demonstrate whether there is a difference between the PDA coating and the PDA film as well as the different sides of the PDA films. Here, the peak intensity ratio of the D-band to that of the G-band (I_D/I_G ratio) was used to show the different chemical and structural information on the PDA coating, airside, and waterside of PDA films (Figure 2B). The highest I_D/I_G ratio band was observed in the airside of the PDA film (I_D/I_G = 0.36), indicating a higher level of oxidation,[18] as compared to the waterside of PDA film (I_D/I_G = 0.32) and the PDA coating (I_D/I_G = 0.18). In the transfer of 2D and quasi-2D films, such as graphene oxide, the transfer methods might result in a difference in the coverage of the materials onto the same substrate due to the different sp^3/sp^2 carbon ratio, which changed the intersheet interactions between the film and the substrate[19] As there is a correlation between the I_D/I_G ratio and the sp^3/sp^2 carbon ratio,[20] the PDA coating, airside, and waterside of PDA films might interact distinctly with the Si/SiO$_2$ wafer surface. Furthermore, the chemical difference between the PDA-functionalized surface was characterized by X-ray photoelectron spectroscopy (XPS), which evidenced the gradually increased polymerization levels from the PDA coating, to the waterside of the PDA film, to the airside of the PDA film (Figure S2, Supporting Information).

Though no difference was observed in the PDA coverage, a divergence in the macroscopic morphology and the intrinsic optical property of PDA modification was visualized under a digital microscope with a 3000 × magnification and SEM (Figure 2C). The difference in the color between the PDA coating and PDA films was partially due to the different PDA thicknesses. While the topographical difference between the waterside and the airside of PDA films that was raised from the presence of the PDA particles as evidenced by SEM, which further led to the changes in the roughness and then caused the changes in the orientation of the PDA film once transferred to the supporting substrate (Figure S3, Supporting Information). Additionally, in contrast to the evenly spread waterside of the PDA film on the wafer, the airside of the PDA film displayed wrinkled structures, as the attached PDA particles affected the interaction between the waterside of the PDA film and the wafer. These together determined the surface hydrophilicity of the PDA-modified surfaces (Figure 2D). The average advancing and receding contact angle (Adv, Rec) decreased from (≈56.1°, ≈37.6°) to (≈14.5°, ≈10.6°) with PDA functionalization.

2.3. Elastic and Adhesive Properties of the PDA-Modified Surfaces

The difference in surface chemical properties and the micro/macroscale structures not only resulted in alterations of the surface hydrophilicity but also yielded changes in the elastic and the adhesive properties of the PDA materials. Understanding their mechanical strength would advance the continuous transfer of the PDA film in a more controlled manner, since a continuous film transfer (≥ 90% coverage) requires the film with a high mechanical strength to remain cohesive during transfer.[21] However, the measured value of the Young's modulus are varied under different measuring conditions. For instance, Klosterman et al.[22] and Li et al.[23] reported Young's modulus of the PDA surface at 2 GPa when using unspecified and a 25 μN applied force, respectively. Lin et al. observed a Young's modulus of the PDA surface at 10 GPa with an applied force of 0.1 mN.[24] With knowledge that absolute value of Young's modulus is hardly comparable between different studies due to the aforementioned aspects, here, we took great care to control environmental conditions during the measurements and avoid any potential plastic deformation due to the penetration of AFM tips into the PDA film or sliding between the tip and the PDA film. A 10 nN load was applied to the surface to measure the Young's modulus of the PDA surfaces using the Quantitative imaging (QI) mode (**Figure 3**A,B). The applied force mimicked the force that a cell can applied to the culture substrate.[25] The unmodified wafer surface was used as a control, which exhibited a Young's modulus of 57.3 ± 7.0 MPa. The stiffness of PDA coating, the waterside, and the airside decreased, which displayed Young's modulus of 6.6 ± 3.1, 24.1 ± 11.8, and 9.3 ± 4.4 MPa. Our result is in line with the one reported by Stöckle et al., of which the apparent Young's modulus of the PDA film was 12.1 ± 1.6 MPa.[26] As compared to the reported multilayered PDA film (13 ± 4 GPa; AFM indentation in air),[11] the prepared PDA film displayed a low modulus of elasticity, flexibility, and bendability, which made it an ideal material for mimicking the natural BM and recapitulating the wrinkling and folding of skin during wound healing and development.

On the other hand, the adhesion of PDA was important for its application, as it influenced the transfer and deposition of PDA materials. Here, by means of AFM adhesion force mapping in the QI mode, each adhesion map includes 16 384 force curves, which allows the evaluation of how surface roughness influences the adhesion behaviors between the AFM tip and the PDA-modified surfaces. The adhesive interaction between the AFM tip and the PDA-functionalized surface was lower compared with those between the AFM tip and the uncoated Si/SiO$_2$ surface (Figure 3C,D). During the force measurements, there was a jump-in behavior when the AFM tip approached the PDA-modified surfaces, demonstrating the attraction force between them. In line with previous reports, the jump-in behavior during the approach is primarily caused by their van der Waals interaction.[27] In aqueous media, van der Waals interactions are weak when surfaces are separated by more than a few nanometers.[28] Thus, during the separation, the adhesion measured is most likely caused by hydrogen
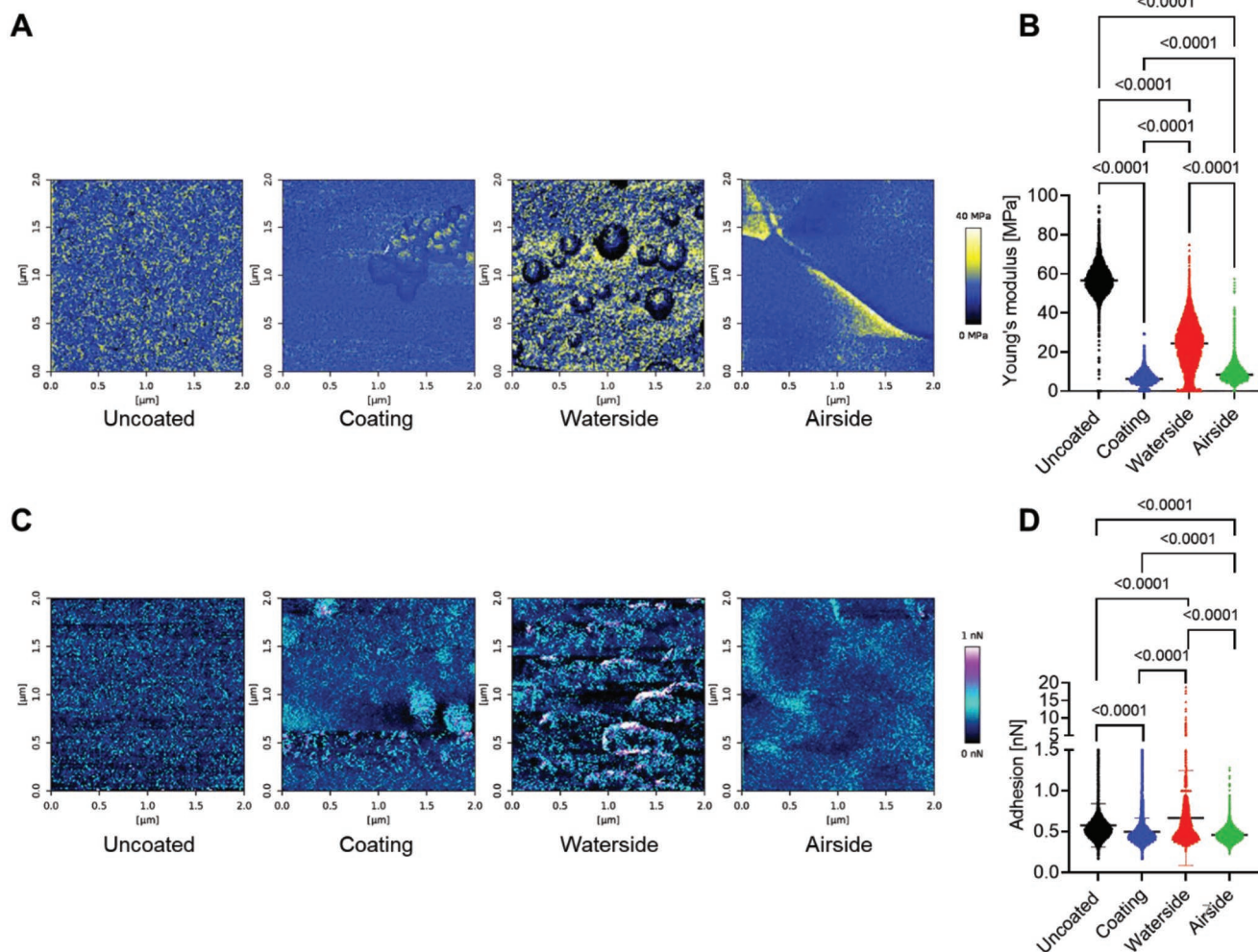
Figure 3. Elastic and adhesive properties of PDA-functionalized surfaces. A) The Young's modulus map (128 pixels × 128 pixels) of the PDA surfaces. B) The measured value of the Young's modulus of the PDA surfaces in QI mode in air (Each bar represents the mean ± SD in one map that includes 16 384 force curves). C) The adhesion map (128 pixels × 128 pixels) of the unmodified or different PDA surfaces. D) Adhesion strength between the AFM tip and the PDA surfaces underwater. (Each bar represents the mean ± SD in one map that includes 16 384 force curves).

bonds and the polarized bond between the silicon AFM tip and the O-containing groups on the target surface.[29] The decreased adhesion on the PDA-modified surface compared to the SiO_2/Si surface might be due to the weakened polarized bond between Si and O-containing groups. On the PDA-modified surfaces, consistent with a previous study,[30] the dispersion of adhesion is higher for the rougher surface, which was observed on the waterside of the PDA film that exhibits the highest dispersion.

2.4. HaCaT Cells Growth on PDA-Functionalized Surfaces

An improved understanding of the structural and mechanical properties of the PDA materials will guide the multiple application of PDA materials for guiding cell behaviors. Here, we started by evaluating the survival and growth of HaCaT cells on PDA-functionalized surfaces. The cell viability on the PDA-functionalized surfaces exhibited no manifest difference after 48 h postseeding (**Figure 4**A). The cell proliferation was evaluated for 7 d (Figure 4B). Of note, HaCaT cells exhibited a comparable growth rate in each group, indicating that the PDA modification did not impair cell proliferation, while the gene expression profile was altered fundamentally by the surface with PDA modification. Specifically, AKT2 and CDC42 were upregulated in cells cultured on the surface with PDA coating; on the waterside of the PDA film, the expression of RAC1 and RAF1 was enhanced; on the airside of the PDA film, the expression of RASA1, MRAS, PIK3CA, AKT3, and MCF2L was increased. Since AKT2 has been identified as strongly expressed by skin basal layer cells, the PDA coating might be able to support the maintenance of HaCaT cells in the basal layer epidermal cells phenotype.[31] The loss of CDC42 could trigger the disruption of apical-basal polarity and impair the cellular mechanosensing.[31]
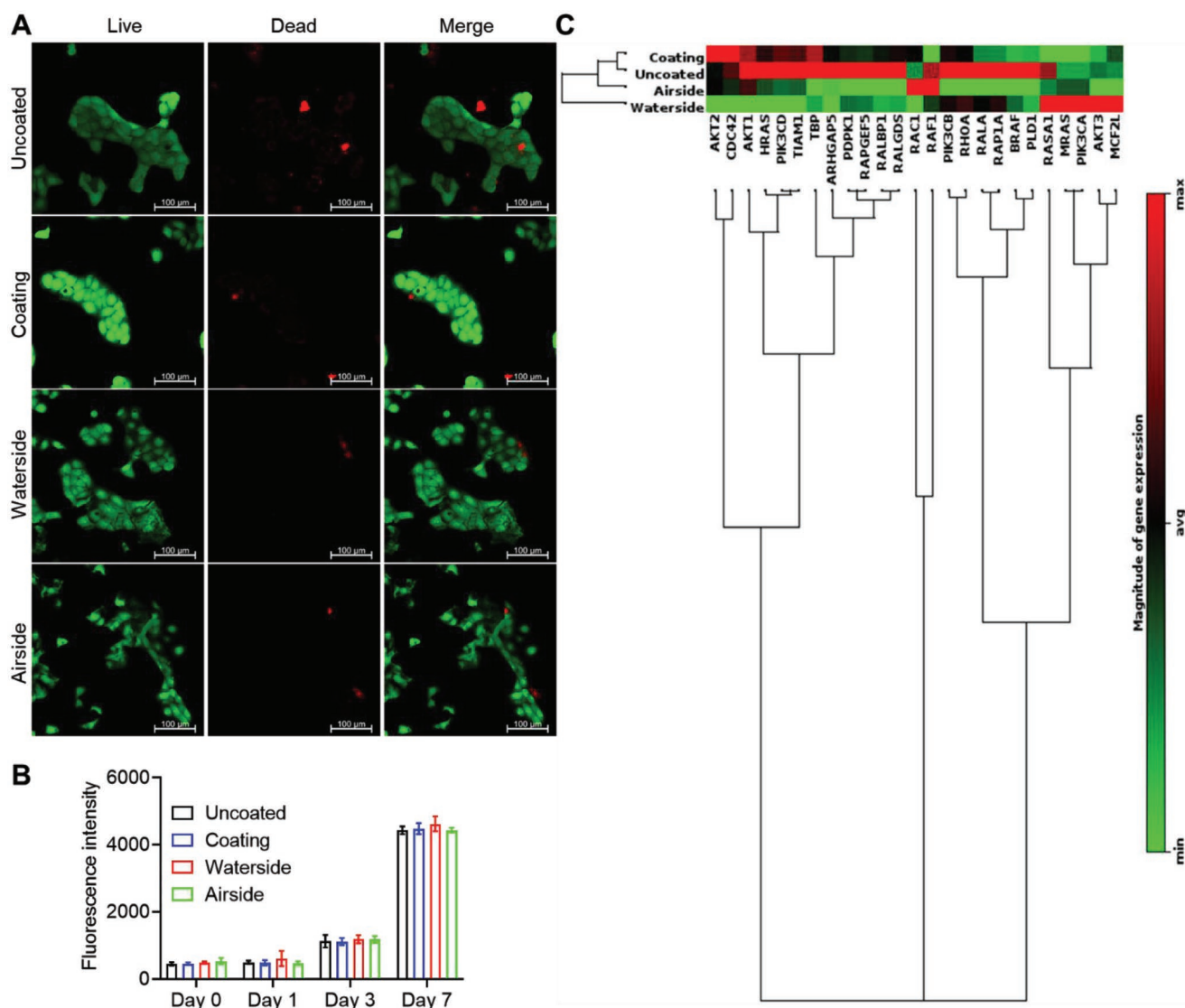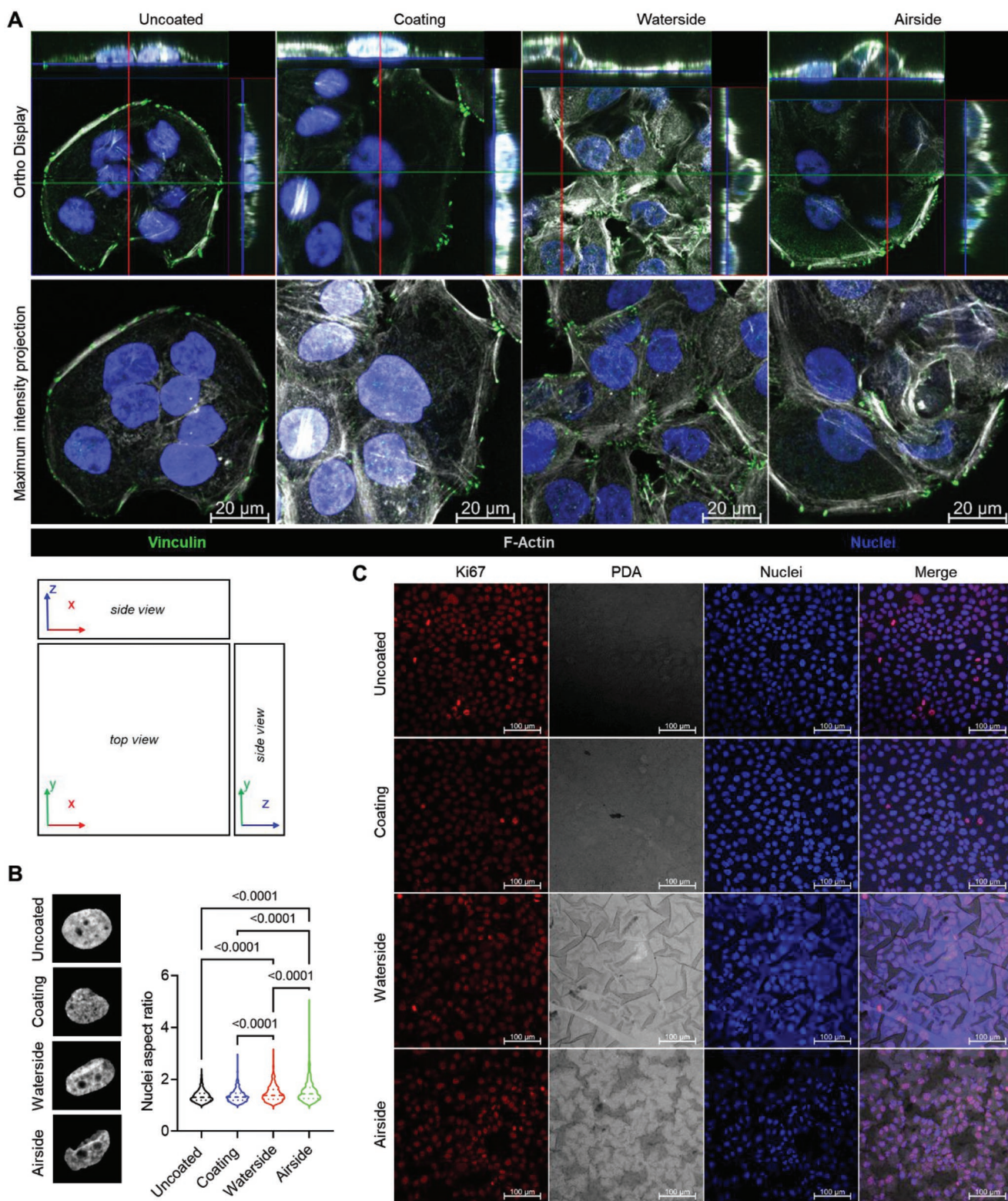
Figure 4. The survival and growth of HaCaT cells on PDA-functionalized substrates. A) Fluorescence images of live (green) and dead (red) HaCaT cells cultured on surfaces with or without PDA modification. Scale bar = 100 µm. B) HaCaT cell proliferation on surface with or without PDA modification. C) Gene expression profile of HaCaT cells cultured on surface with or without PDA modification. Clustering analysis of the expression of genes related to the crosstalk between Ras-family GTPases.

This together indicated that the PDA coating was able to regulate the homeostasis of the skin. In cells grown on the waterside, RAC1 and RAF1 are involved in the activation of the mitogen-activated protein kinase kinase/extracellular signal-regulated kinase (MEK-ERK) signaling cascade, which regulates cellular growth, differentiation, and apoptosis.[32] Since proliferation/differentiation processes of keratinocytes are essential to skin morphogenesis,[33] studying interactions between HaCaT cells and the waterside of PDA film would provide insights into the skin morphogenesis as well as epithelial deformation and folding due to body movement. Yet the hidden functions of the airside of PDA film need to be further investigated, as genes involved in multiple signals were upregulated.

2.5. Interaction between the PDA Materials and Cells

The optical sectioning capacity provided by the laser-scanning confocal microscope (LSCM) allows the observation of the entire volume of the 3D cell sheet based on the front view and the side view. Altered cell shape and organization as well as the interaction between Vinculin and F-actin were visualized through immunofluorescence staining (**Figure 5**A). On the uncoated surface and PDA coating, HaCaT cells were grown as a flat monolayer, of which cells were firmly attached to those substrate surfaces. In contrast, the cell sheet deformation was observed in cells grown on both waterside and airside of the PDA film, which formed multicellular dome-shaped structures

**ADVANCED
SCIENCE NEWS**

www.advancedsciencenews.com

**ADVANCED
MATERIALS
INTERFACES**

www.advmatinterfaces.de

Figure 5. Interaction between PDA materials and HaCaT cells. A) Influence of PDA modification on the interaction between Vinculin and F-actin in HaCaT cells. Cell sheet and distribution of Vinculin and F-actin were visualized based on the front view (upper panel) and the side view (lower panel). Focal adhesion complexes were stained with anti–Vinculin antibody (green), actin was labeled with phalloidin (white), and nuclei were counterstained with DAPI (blue). Scale bar = 20 μm. B) Nuclei deformation caused by PDA modification. Representation nucleus image was shown in the left panel. Nuclei aspect ratio was analyzed using automated image analysis algorithm in image J and shown in the right panel (the number of nuclei analyzed in each group: Uncoated, $n = 1157$, Coating, $n = 798$, Waterside, $n = 757$, Airside, $n = 877$). C) HaCaT cell-induced deformation and delamination of PDA materials. Representative images of PDA materials (gray) and HaCaT cells stained for Ki67 (red) and nuclei (blue). Scale bar = 100 μm.

**ADVANCED
SCIENCE NEWS**
www.advancedsciencenews.com

**ADVANCED
MATERIALS
INTERFACES**
Open Access
www.advmatinterfaces.de

according to the side-view images. In addition, the deformation of nuclei occurred and the level of nuclei deformation was determined by evaluating the aspect ratio (Figure 5B). The difference in the nucleus shape echoed the altered gene expression in cells grown on different PDA materials, as the nucleus shape is closely related to cellular processes and signaling transduction.[34] To check whether the PDA film that served as the BM mimics could also be deformed by the cells, the PDA materials were labeled with a fluorescence dye, as light microscopy offers a versatile platform to acquire such information with high spatiotemporal resolution. Deformation and delamination of the PDA films were observed at spatial scales from micrometers to millimeters (Figure 5C). Together, the LSCM was applied to monitor the shape dynamics of cells as well as the cell-induced deformation of the PDA materials. This approach would deepen our understanding of tissue morphogenesis since it highly relies on observing cell shape changes, cell-cell interactions, and cell-BM interactions. Moreover, the observation of these dynamic behaviors requires the methods and model to monitor morphological alterations at both the single-cell and tissue levels. Though curved substrates and elastomers have been employed to investigate the deformation and folding of cells and the BM mimics, it was still limited by the rigid substrate that cells and BM mimic attached to. It is essential to develop new in vitro models for an advanced understanding of epithelial morphogenesis and its functions.

2.6. In Vitro Freestanding Model of Epithelium-BM Interactions

In order to gain more insights into their interactions, the possibility of forming an epithelium-BM mimic made of the PDA film and HaCaT cells was probed. It is envisioned that the higher binding force between cells and BM would favor the folding and deformation of the biohybrid. Thus, the binding force between an HaCaT cell and the PDA materials was measured using AFM (**Figure 6**A). The highest binding force was detected between the cell and the waterside of PDA film (2.37 ± 0.57 nN). Considering the asymmetrical distribution of extracellular matrix components to the epithelial and the stromal side, the unique sidedness of PDA film made it more similar to the natural BM.[1b] Accordingly, the waterside of the PDA film was selected to establish the in vitro freestanding model for the study of epithelial-BM interactions. To prove the concept, the mechanical strength of the freestanding PDA film was next determined by the AFM nanoindentation at room temperature underwater (Figure 6B). As compared to the area with a supporting substrate, the apparent Young's modulus of the suspended PDA film over open squares was lower, which represented the intrinsic stiffness of the PDA film (Figure 6C). It should be noted that this intrinsic stiffness and the thickness of the PDA film showed similarity in comparison to the human native basal membrane (≈1.0 MPa, ≈100 nm in thickness).[35] As evidenced by the SEM (Figure 1A), the PDA film displayed high flexibility and could be deformed without cracking, which makes the PDA film of high potential for mimicking the epithelial wrinkling and folding. Our result confirmed that the freestanding PDA film could support the growth of the epithelial cells and was able to be deformed by the cells (Figure 6D),

which may be attributed to the cell-generated forces, such as cell-cell and cell-substrate adhesion forces as well as forces resulting from the plasma membrane tension and actomyosin contractility.[36] Altogether, the flat PDA-cell biohybrid system could actively be deformed and curled into a 3D structure that showed similarity to the normal human skin tissue (Figure 6E). As the PDA films are mimics of natural BM, our results could be used to improve the understanding of the mechanism involved in epithelial wrinkling and folding (Figure 6F,G and siVideo). These data can also be applied for the training of computational approaches and the evaluation of the fitness of the models of biological structural changes.[36b,37] Yet, it is still challenging to interpret and convert these results into biological understandings.

3. Conclusion

The interactions between the BM and epithelial cells are important for tissue morphogenesis and biofunctions, yet effort to study those processes is hampered by the lack of models that recapitulate the asymmetrical structure and the mechanics of the BM. Here, we applied the PDA-based material as a BM mimic for the study of cell-BM interactions in vitro. Compared to the PDA coating that formed at the L/S interface, the PDA film assembled at the A/L interface was able to be deformed and delaminated by the skin epithelial cells. Of note, HaCaT cells were able to distinguish the asymmetry of the two opposing sides of the PDA film, of which cells exhibited a stronger adhesion affinity to the waterside of PDA film. Thus, a freestanding cell-PDA hybrid could be efficiently acquired based on the adhesion between cells and the waterside of PDA films. It allowed the visualization of cell dynamics from micro- to millimeter scales without the restrictions from the rigid culture substrate. In this freestanding system, cells drove the deformation of the cell-PDA complex, which displayed the autonomous formation of complex 3D structures that mimic in vivo-relevant folding events. Since the development of biomimetic in vitro models is crucial for understanding tissue maturation and function, studying this process in vitro would help to understand the tissue folding during development and provide insights into engineering strategies for tissue regeneration.

4. Experimental Section

Substrate Functionalization with PDA: PDA-functionalized substrates were acquired at either the L/S or the A/L interface. Dopamine hydrochloride (DA, Sigma-Aldrich, Germany) was dissolved in a sterile 50 mM Tris-HCl buffer at pH 8.5 (Jena Bioscience GmbH, Germany) at a concentration of 2.0 mg mL^{-1}. The polymerization process was conducted in the absence of mechanical stimulus in a beaker with a nonsealed coverlid for 24 h. To form the PDA coating, substrates were immediately immersed in the solution at the beginning of the reaction and lasted for 24 h. To functionalize the substrates with PDA film, the Langmuir Transfer technique was applied at the A/L interface 24 h after the polymerization reaction started. Specifically, Langmuir technology was applied to allow the attachment of either the waterside or the airside of the PDA film to the substrates, such as the thermal oxide silicon wafer (Si/SiO$_2$ wafer, Sil'tronix Silicon Technologies, France). After air drying overnight, the resulting PDA materials were rinsed with the
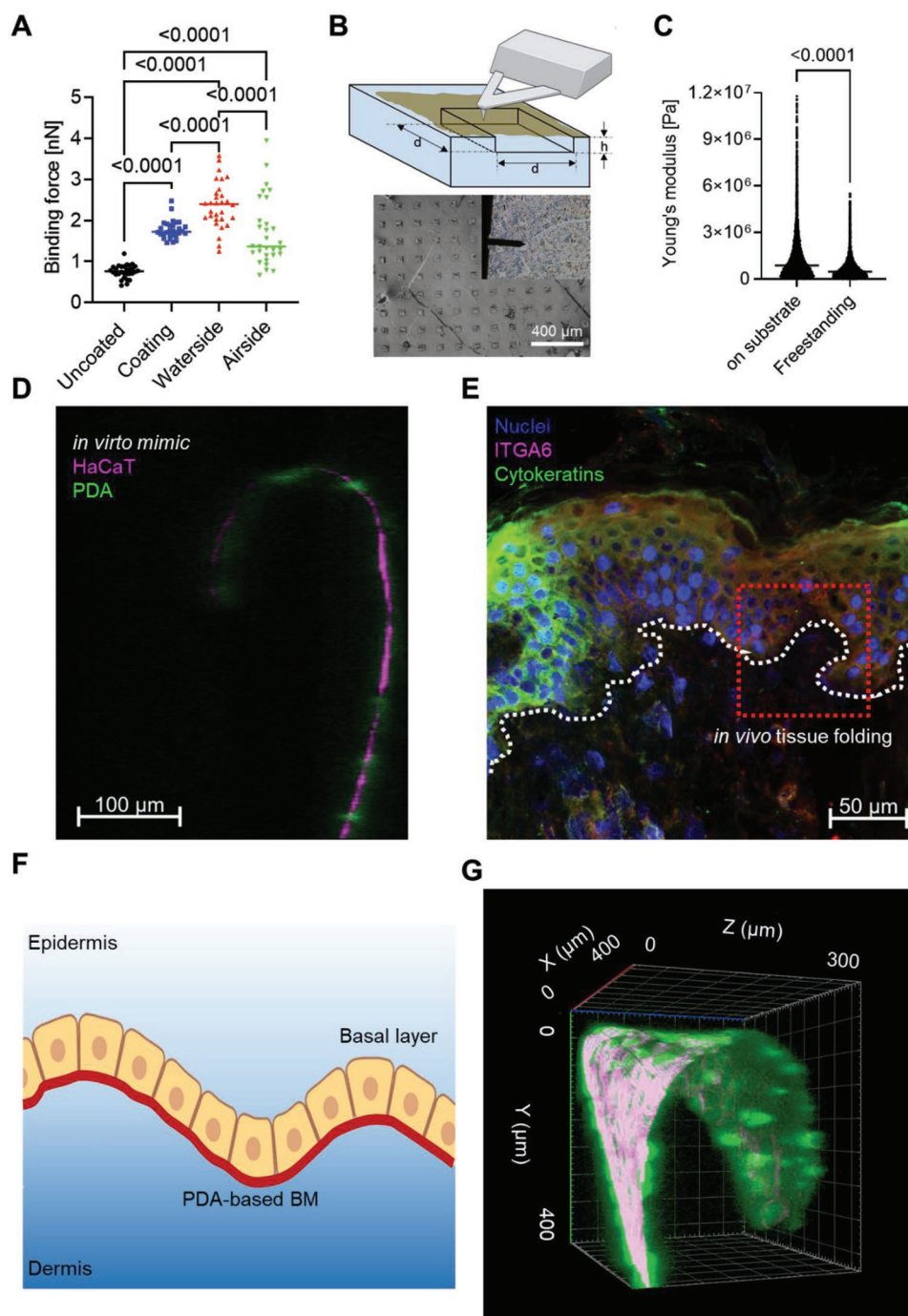
Figure 6. PDA-based BM-epithelium model. A) AFM measurement of live cell-surface binding force. (*n* = 30). B) Schematic and bright-field image of AFM force mapping on the freestanding PDA film suspended over a polystyrene substrate with square concaves (*d* = 50 µm, *h* = 10 µm). The waterside of PDA film was presented to the AFM probe. C) Young's modulus of the waterside of PDA film with or without the support from the substrate. D) Cross-sectional view of the freestanding biohybrid system made of the PDA film and HaCaT cells. HaCaT cells stained for F-actin (magenta), and PDA was labeled with NHS-Fluorescein (green). Scale bar = 100 µm. E) Immunofluorescence staining of health human full-thickness skin. The dermis is connected to the epidermal layers at the level of the basement membrane, where white dash lines indicated the epidermal-dermal boundary, basement membrane (BM). Cells stained for Cytokeratins (green), ITGA6 (magenta), and nuclei (blue). Scale bar = 50 µm. F) Cross-sectional view of the in vitro model based on basal layer of epithelial cells and PDA film. G) 3D reconstruction of basal layer of epithelial cells-BM model. HaCaT cells stained for F-actin (magenta), and PDA was labeled with NHS-Fluorescein (green).

Millipore water to wash off the loosely combined PDA particles. Then resulting PDA materials were air-dried overnight again and were ready for downstream characterization.

Characterization of PDA-Functionalized Substrates: The thickness and the surface morphology of the PDA layer and its mechanical properties were measured using an AFM (NanoWizard 4 BioAFM, JPK

Instruments, Bruker, Germany). The thermal noise-based calibration was performed to acquire the spring constant of the cantilever before each experiment.[38] For measuring the thickness and the surface morphology of PDA material, a 2.0 N m^{-1} tetrahedral AFM tip with a nominal resonant frequency of 70 kHz (OPUS-240AC-NG, NanoAndMore GMBH, Germany) was used. By keeping the oscillation amplitude at the first cantilever eigenmode constant with height displacement, surface topography was recorded in the A/C mode in the air at room temperature. For measuring the apparent Young's modulus of the PDA-functionalized surfaces, a 2.0 N m^{-1} tetrahedral AFM tip with a nominal resonant frequency of 70 kHz (OPUS-240AC-NG, NanoAndMore GMBH, Germany) was used in the QI mode. At room temperature, the apparent Young's modulus was measured at a load = 10 nN to avoid the substrate effect. The adhesion properties of the PDA material were measured using a 2.0 N m^{-1} tetrahedral AFM tip with a nominal resonant frequency of 70 kHz (OPUS-240AC-NG, NanoAndMore GMBH, Germany) underwater at room temperature. The QI mode with a resolution of 128 pixels × 128 pixels and the scan size was set as 2.0 μm × 2.0 μm. A load = 10 nN was used to acquire the force spectroscopy at each pixel. The baseline was adjusted to correct for any changes in the setpoint. Data were processed using the JPK scanning probe microscopy (JPKSPM) Data processing software (JPK Instruments, Bruker, Germany).

The Raman analysis was performed using a Confocal Raman Microscope (SENTERRA II Raman Microscope, Bruker Optik GmbH, Germany). A laser beam at $\lambda = 532$ nm was used as excitation light source. The scattered light from the sample was collected with an objective at 50 times magnification. An average of 64 cycles was used to increase signal to noise ratio. Spectra analysis was conducted using ORIGIN 2021 (OriginLab Corporation, US). Raman spectra were normalized by the maximum intensity of each spectrum in the range of [0, 1].

XPS measurements were performed using a KRATOS AXIS Ultra DLD (Kratos Analytical, Manchester, United Kingdom) equipped with a monochromatic Al Kα anode working at 15 kV (180 W). For the survey spectra, a pass energy of 160 eV was used while for the region spectra, the pass energy was 20 eV. The investigated area was 700×300 μm^2. The evaluation and validation of the data were carried out with the software CASA-XPS version 2.3.25. Calibration of the spectra was done by adjusting the C1s signal to 284.8 eV. For deconvolution of the region files, background subtraction (linear or Shirley) was performed before calculation.

The macroscopic morphology of the PDA-functionalized surface was observed using a digital microscope (VHX-100, KEYENCE DEUTSCHLAND GmbH) at 3000 times magnification. The hydrophilicity of the PDA-functionalized substrate surfaces was determined by measuring the water contact angle using the captive bubble method at room temperature with a drop shape analyzer 100S (DSA100S) (Krüss Optronic GmbH, Germany).

SEM (Supra 40 VP, Carl Zeiss, Germany) was conducted to analyze the topography of the PDA-functionalized surfaces in the dry state. SEM images of the morphologies of the PDA-functionalized surfaces were obtained using both in-lens (SE1) and Everhart-Thornley detector (or SE2) detectors and analyzed at 3 keV acceleration voltage.

Maintenance of HaCaT Cells: The human keratinocyte cells, HaCaT cells (purchased from American Type Culture Collection (ATCC), USA), were maintained in Dulbecco's modified Eagle's medium (Thermo Fisher Scientific, Germany) supplied with 10% v/v fetal bovine serum (Sigma-Aldrich, Germany), 100 U mL^{-1} Penicillin-Streptomycin medium (Thermo Fisher Scientific, Germany). Cells were passaged when reaching ≈80% confluence at a ratio of 1:6 for expansion. The influence of PDA modification on cell viability was evaluated using a LIVE/DEAD Viability/Cytotoxicity Assay Kit (Thermo Fisher Scientific, Germany).

Cell Proliferation Assay: The proliferation of cells was studied by the measurement of cell number. Briefly, the growth of the HaCaT cells on the PDA-functionalized surfaces was determined by counting the number of adherent cells using the Blue Fluorometric dsDNA Quantitation Kit (Thermo Fisher Scientific, Germany). HaCaT cells were seeded at a density of 5×10^3 cells cm^{-2} and were collected on Day 0, Day 1, Day 4, and Day 7 to acquire the cell lysate. Then cellular lysates were incubated

with the probe and the fluorescence was measured using excitation and emission filters centered at 360 and 460 nm, respectively, with a microplate reader (Infinite 200 Pro, Tecan Group Ltd. Switzerland).

Gene Expression Analysis: Briefly, mRNA was isolated using a TRIzol Reagent (Thermo Fisher Scientific, Germany) follow by the synthesis of cDNA using a RevertAid RT Reverse Transcription Kit (Thermo Fisher Scientific, Germany). The influence of PDA modification on cellular gene expression was detected using a PrimePCR Array target to the Crosstalk between Ras-family GTPases (Bio-Rad Laboratories, Germany).

Immunofluorescence Staining: The human frozen tissue section was purchased from AMS Biotechnology (AMSBIO) (Specimen ID: 057-106 Skin) and stained with antibodies against ITGA6 and Cytokeratins (Thermo Fisher Scientific, Germany). Cells were fixed with 4% w/v paraformaldehyde (Sigma-Aldrich, Germany) and permeabilized with 0.2% Triton X-100 (v/v, Sigma-Aldrich, Germany). After blocking with 4% v/v goat serum (Thermo Fisher Scientific, Germany), cells were stained with primary antibodies, including, Anti-Vinculin (Thermo Fisher Scientific, Germany) and Ki67 (Cell Signaling Technology, Germany) at 4 °C overnight. Then secondary antibody (Thermo Fisher Scientific, Germany) staining was performed at room temperature for 1 h. F-actin was stained using ActinRed 555 ReadyProbes (Thermo Fisher Scientific, Germany). Nuclei were counterstained with DAPI (4',6-diamidino-2-phenylindol, Thermo Fisher Scientific, Germany) or NucRed Dead 647 ReadyProbes (Thermo Fisher Scientific, Germany). A laser scanning confocal microscope (LSM780, Carl Zeiss, Germany) was used to acquire images. The orthogonal view and 3D reconstruct of cells and cell-PDA hybrids were generated based on the confocal Z-stacks of fluorescence images. To visualize the PDA film under a fluorescence microscope, PDA film was labeled with *N*-hydroxy-succinimidyl-ester (NHS)-Fluorescein (Thermo Fisher Scientific, Germany) at pH = 7.0 in room temperature for 30 min.

AFM-Based Single-Cell Force Spectroscopy: The single HaCaT cells were acquired by dissociating the cells with Trypsin-ethylenediaminetetraacetic acid (EDTA) (0.25%, v/v Thermo Fisher Scientific, Germany). To capture a single HaCaT cell onto the tip-less AFM cantilever (ARROW-TL2Au, NanoAndMore GmbH, Germany), the single-cell suspension was placed into a Petri Dish (Thermo Fisher Scientific, Germany) that was pre-treated with bovine serum albumin (Sigma-Aldrich, Germany). A contact force of 5.0 nN was applied by the CellHesion200 atomic force microscope system (JPK Instruments, Bruker, Germany) onto a single HaCaT cell for 10 s, which allowed the cell to firmly attach to the tip-less AFM cantilever. The cellular adhesion force was determined by retracting the cantilever-bound cell from the substrate surface. During this process, the height position and deflection of the cantilever were recorded as a function of time. The force spectroscopy was used to calculate the strength of cell adhesion to substrates using the JPKSPM Data processing software (JPK Instruments, Bruker, Germany).

Statistical Analysis: The number of replications is indicated in the figure legends for each experiment. Data were expressed as mean value ± standard deviation (SD). All experiments were repeated at least three times, and data are presented as mean ± SD. Statistical analysis was performed using one-way analysis of variance (ANOVA) followed by Tukey's test with GraphPad Prism v9.1 software (GraphPad, USA). A *p*-value less than 0.05 was considered statistical significance.

Supporting Information

Supporting Information is available from the Wiley Online Library or from the author.

Acknowledgements

2202509 (10 of 11)

Conflict of Interest

The authors declare no conflict of interest.

Data Availability Statement

The data that support the findings of this study are available from the corresponding author upon reasonable request.

Keywords

[1] a) D. Breitkreutz, N. Mirancea, R. Nischt, *Histochem. Cell Biol.* **2009**, *132*, 1; b) R. Jayadev, D. R. Sherwood, *Curr. Biol.* **2017**, *27*, R207.

[2] E. Roig-Rosello, P. Rousselle, *Biomolecules* **2020**, *10*, 1607.

[3] a) R. Huang, Z. He, Y. Bian, Z. Lei, H. Wang, Y. Long, M. Hu, J. Li, L. Xu, J. Li, *J. Biomed. Nanotechnol.* **2019**, *15*, 2332; b) E. Groppa, P. Martini, N. Derakhshan, M. Theret, M. Ritso, L. W. Tung, Y. X. Wang, H. Soliman, M. S. Hamer, L. Stankiewicz, *Cell Rep.* **2023**, *42*, 112051.

[4] a) A. Nishiguchi, S. Singh, M. Wessling, C. J. Kirkpatrick, M. Möller, *Biomacromolecules* **2017**, *18*, 719; b) P. Jain, S. B. Rauer, M. Möller, S. Singh, *Biomacromolecules* **2022**, *23*, 3081.

[5] J. C. Selby, M. A. Shannon, *J. Biochem. Biophys. Methods* **2008**, *70*, 932.

[6] A. J. Hughes, H. Miyazaki, M. C. Coyle, J. Zhang, M. T. Laurie, D. Chu, Z. Vavrušová, R. A. Schneider, O. D. Klein, Z. J. Gartner, *Dev. Cell* **2018**, *44*, 165.

[7] J. Peng, M. Grayson, G. J. Snyder, *Matter* **2021**, *4*, 2694.

[8] a) W. Halfter, P. Oertle, C. A. Monnier, L. Camenzind, M. Reyes-Lua, H. Hu, J. Candiello, A. Labilloy, M. Balasubramani, P. B. Henrich, *FEBS J.* **2015**, *282*, 4466; b) M. A. Morrissey, D. R. Sherwood, *J. Cell Sci.* **2015**, *128*, 1661. c) N. Khalilgharibi, Y. Mao, *Open Biol.* **2021**, *11*, 200360.

[9] Z. Deng, W. Wang, X. Xu, Y. Nie, Y. Liu, O. E. Gould, N. Ma, A. Lendlein, *ACS Appl. Mater. Interfaces* **2021**, *13*, 10748.

[10] a) B. O. Okesola, A. Mata, *Chem. Soc. Rev.* **2018**, *47*, 3721; b) A. Levin, T. A. Hakala, L. Schneider, G. J. Bernardes, E. Gazit, T. P. Knowles, *Nat. Rev. Chem.* **2020**, *4*, 615.

[11] E. Coy, I. Iatsunskyi, J. C. Colmenares, Y. Kim, R. Mrówczyński, *ACS Appl. Mater. Interfaces* **2021**, *13*, 23113.

[12] H.-C. Yang, Q.-Y. Wu, L.-S. Wan, Z.-K. Xu, *Chem. Commun.* **2013**, *49*, 10522.

[13] J. Jiang, L. Zhu, L. Zhu, B. Zhu, Y. Xu, *Langmuir* **2011**, *27*, 14180.

[14] J. H. Ryu, P. B. Messersmith, H. Lee, *ACS Appl. Mater. Interfaces* **2018**, *10*, 7523.

[15] F. Ponzio, P. Payamyar, A. Schneider, M. Winterhalter, J. r. m. Bour, F. Addiego, M.-P. Krafft, J. Hemmerle, V. Ball, *J. Phys. Chem. Lett.* **2014**, *5*, 3436.

[16] D. Mallinson, A. B. Mullen, D. A. Lamprou, *J. Mater. Sci.* **2018**, *53*, 3198.

[17] M. L. Alfieri, R. Micillo, L. Panzella, O. Crescenzi, S. L. Oscurato, P. Maddalena, A. Napolitano, V. Ball, M. d'Ischia, *ACS Appl. Mater. Interfaces* **2017**, *10*, 7670.

[18] H. Li, N. Cheng, Y. Zheng, X. Zhang, H. Lv, D. He, M. Pan, F. Kleitz, S. Z. Qiao, S. Mu, *Adv. Energy Mater.* **2013**, *3*, 1176.

[19] R. Hidalgo, D. Lopez-Diaz, M. M. Velázquez, *Langmuir* **2015**, *31*, 2697.

[20] a) A. S. Rudenkov, A. V. Rogachev, A. N. Kupo, P. A. Luchnikov, N. Chicherina, presented at Mater. Sci. Forum, Singapore, October **2019**; b) J. Li, S. J. Kim, S. Han, H. Chae, *Surf. Coat. Technol.* **2021**, *422*, 127514.

[21] K. L. Harrison, L. B. Biedermann, K. R. Zavadil, *Langmuir* **2015**, *31*, 9825.

[22] L. Klosterman, Z. Ahmad, V. Viswanathan, C. J. Bettinger, *Adv. Mater. Interfaces* **2017**, *4*, 1700041.

[23] H. Li, J. Xi, Y. Zhao, F. Ren, *MRS Adv.* **2019**, *4*, 405.

[24] S. Lin, C.-T. Chen, I. Bdikin, V. Ball, J. Grácio, M. J. Buehler, *Soft Matter* **2014**, *10*, 457.

[25] W. J. Polacheck, C. S. Chen, *Nat. Methods* **2016**, *13*, 415.

[26] B. Stöckle, D. Y. W. Ng, C. Meier, T. Paust, F. Bischoff, T. Diemant, R. J. Behm, K. E. Gottschalk, U. Ziener, T. Weil, presented at Macromol. Symp, Mainz, Germany, September **2014**.

[27] a) C. Lim, J. Huang, S. Kim, H. Lee, H. Zeng, D. S. Hwang, *Angew. Chem., Int. Ed.* **2016**, *55*, 3342; b) B. P. Lee, P. B. Messersmith, J. N. Israelachvili, J. H. Waite, *Annu. Rev. Mater. Res.* **2011**, *41*, 99.

[28] C. Zhang, L. Gong, L. Xiang, Y. Du, W. Hu, H. Zeng, Z.-K. Xu, *ACS Appl. Mater. Interfaces* **2017**, *9*, 30943.

[29] J. Onoda, M. Ondráček, P. Jelínek, Y. Sugimoto, *Nat. Commun.* **2017**, *8*, 15155.

[30] A. Alam, M. Howlader, M. Deen, *J. Micromech. Microeng.* **2014**, *24*, 035010.

[31] A. Elbediwy, Z. I. Vincent-Mistiaen, B. Spencer-Dene, R. K. Stone, S. Boeing, S. K. Wculek, J. Cordero, E. H. Tan, R. Ridgway, V. G. Brunton, *Development* **2016**, *143*, 1674.

[32] M. D. Mazalouskas, R. Godoy-Ruiz, D. J. Weber, D. B. Zimmer, R. E. Honkanen, B. E. Wadzinski, *J. Biol. Chem.* **2014**, *289*, 4219.

[33] a) W. T. Gibson, M. C. Gibson, *Curr. Top. Dev. Biol.* **2009**, *89*, 87; b) A. Mieremet, R. van Dijk, W. Boiten, G. Gooris, J. A. Bouwstra, A. El Ghalbzouri, *J. Tissue Eng. Regener. Med.* **2019**, *13*, 1122.

[34] C. S. Janota, F. J. Calero-Cuenca, E. R. Gomes, *Curr. Opin. Cell Biol.* **2020**, *63*, 204.

[35] a) A. N. Kozyrina, T. Piskova, J. Di Russo, *Front. Bioeng. Biotechnol.* **2020**, *8*, 1255; b) J. Candiello, G. J. Cole, W. Halfter, *Matrix Biol.* **2010**, *29*, 402.

[36] a) D. N. Clarke, A. C. Martin, *Curr. Biol.* **2021**, *31*, R667; b) Y. Kobayashi, Y. Yasugahira, H. Kitahata, M. Watanabe, K. Natsuga, M. Nagayama, *npj Comput. Mater.* **2018**, *4*, 45; c) C. Simon, R. Kusters, V. Caorsi, A. Allard, M. Abou-Ghali, J. Manzi, A. Di Cicco, D. Lévy, M. Lenz, J.-F. Joanny, *Nat. Phys.* **2019**, *15*, 602.

[37] D. Pastor-Escuredo, J. C. del Álamo, *Front. Phys.* **2020**, *8*, 31.

[38] R. E. Iv, T. Camesano, *Ultramicroscopy* **2006**, *106*, 413.